iScience

CellPress
OPEN ACCESS

Article

Gradient phase and amplitude errors in atomic magnetic gradiometers for biomagnetic imaging systems

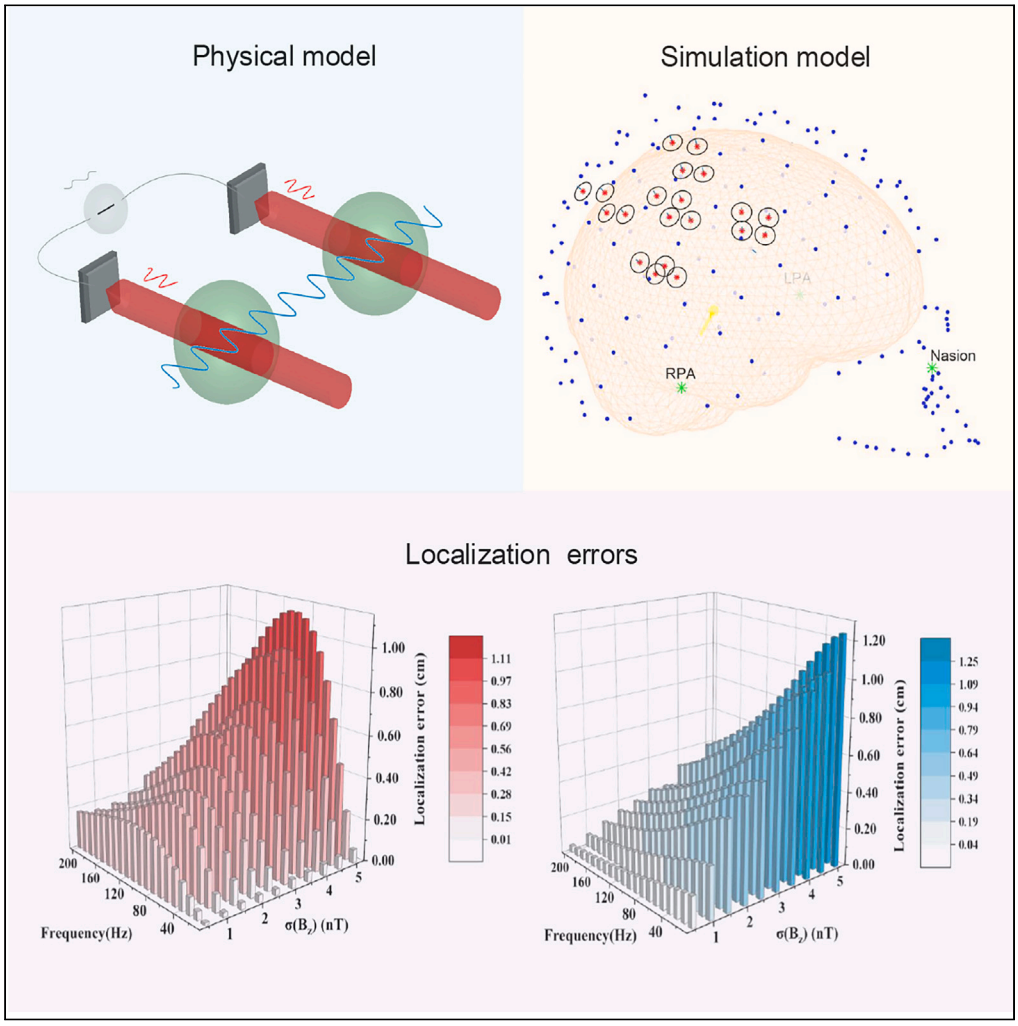

Ziqi Yuan, Shudong Lin, Ying Liu, Junjian Tang, Tengyue Long, Yueyang Zhai

liu_ying@buaa.edu.cn (Y.L.)
yueyangzhai@buaa.edu.cn (Y.Z.)

Highlights

First observation of gradient phase and amplitude errors in OPM gradiometers

The errors are frequency dependent

Theory and experiments demonstrate the impacts of key parameters on the performance

The source localization error of MEG is simulated

Yuan et al., iScience 27, 109250
March 15, 2024
https://doi.org/10.1016/j.isci.2024.109250

iScience

CellPress
OPEN ACCESS

Article

Gradient phase and amplitude errors in atomic magnetic gradiometers for biomagnetic imaging systems

Ziqi Yuan,[1,2] Shudong Lin,[1,2] Ying Liu,[1,2,4,5,*] Junjian Tang,[1,2,3] Tengyue Long,[1,2] and Yueyang Zhai[1,2,4,*]

SUMMARY

The cross-axis projection error (CAPE) caused by residual magnetic fields has recently attracted widespread attention. In this study, we propose a more specific theoretical model and expand the CAPE in gradient measurements. We first report that differences in relaxation rate and residual magnetic field between optically pumped magnetometers (OPMs) introduce a significant error term in the output of OPM gradiometers, referred to as the gradient phase error. Furthermore, when the longitudinal field compensation is inadequate, the interaxial response interference of a single OPM is prominent, resulting in an amplitude distortion of the signal. This is further amplified in the gradiometer configuration, introducing the gradient amplitude error. Our experiments demonstrated that the efficacy of mitigating common-mode noise of OPM gradiometers was significantly impaired when existing the gradient errors. In addition, a simulation with a magnetoencephalography (MEG) system illustrated an induced source localization error of exceeding 2 cm, severely compromising the localization accuracy of OPM-MEG systems.

INTRODUCTION

Magnetoencephalography (MEG) and magnetocardiography (MCG) are noninvasive imaging techniques for biomagnetic fields.[1–5] Superconducting quantum interference devices (SQUIDs) and optically pumped magnetometers (OPMs) are considered as the main means of performing MEG and MCG.[6–8] To eliminate the influence of environmental magnetic field drift[9] and suppress the intrinsic noise of the measurement system,[10] a magnetic gradiometer configuration has been proposed that effectively guarantees the reliability and accuracy of multi-channel MEG and MCG systems.[11,12] Gradiometers implemented using SQUIDs have been developed for several decades, and multi-channel OPM gradiometers have also been widely applied in recent years.[13–15] Instead of coupling weak magnetic fields to low Tc SQUIDs via pickup coils,[16] OPMs utilize the thermal atomic ensembles to perform magnetic field measurements.[17,18] By eliminating the bulky dewar used to insulate between the cryogenic liquid nitrogen from the subject's skin, OPMs are more flexible and portable, requiring lower construction and maintenance costs.[19,20] More importantly, closer spacing between channels and smaller distances from subjects make OPMs more effective in terms of their better spatial-resolution and higher signal-to-noise ratio.[21]

Researchers have made remarkable achievements in the structural design of the OPM array to enhance the source localization capabilities of the OPM-MEG and OPM-MCG systems. Multiple designs of multi-channel configuration in a single vapor cell have been proposed for *in-situ* gradient measurements and gradient magnetic field compensation.[22,23] However, they are limited in actual applications because of their inflexibility and the difficulty of adjusting their locations. To combine the properties of flexibility and miniaturization, multi-channel designs with multiple vapor cells have been developed for high-resolution gradient measurements of fetal MCG (fMCG) and adult MEG systems.[20,24,25] These structures allow more channels to be arranged in a limited space, facilitating the flexible configuration of OPM gradiometers. Magnetic gradiometers are typically implemented by subtracting the measurement signals of two adjacent magnetometers through post-processing to suppress common-mode noise.[26] Thus, high common-mode rejection ratio (CMRR) requires high consistency between channels. The consistency of different probes in SQUIDs systems is usually limited by hand-wound coils.[27] Unlike SQUIDs, the output of OPMs includes ambient-field related terms,[28] and their sensing axes are susceptible to environmental field changes.[1] Furthermore, the increase in array density necessitates the consideration of coupling between channels, including analysis of factors such as the crosstalk of the modulation field in typical single-beam SERF OPMs,[29] and the crosstalk of the static magnetic field generated by three-axis magnetic

[1]Key Laboratory of Ultra-Weak Magnetic Field Measurement Technology, Ministry of Education, School of Instrumentation and Optoelectronic Engineering, Beihang University, Beijing 100191, China
[2]Zhejiang Provincial Key Laboratory of Ultra-Weak Magnetic-Field Space and Applied Technology, Hangzhou Innovation Institute, Beihang University, Hangzhou 310051, China
[3]School of Physics, Beihang University, Beijing 100191, China
[4]Hefei National Laboratory, Hefei 230088, China
[5]Lead contact
*Correspondence: liu_ying@buaa.edu.cn (Y.L.), yueyangzhai@buaa.edu.cn (Y.Z.)
https://doi.org/10.1016/j.isci.2024.109250

compensation coils.[30–32] All of these factors ultimately lead to measurement errors that are large enough to distort the difference signals and yield inaccurate positioning results.[33] Therefore, configuring OPMs as magnetic gradiometers with high CMRR remains a challenge.

The output gain errors drifted by the ambient field and the cross-axis projection error (CAPE)[1] in the presence of a residual static magnetic field have previously been theoretically and experimentally analyzed. Jiang et al. observed and analyzed the relationship between the CAPE and the frequency of the external magnetic field signals of interest in dual-beam OPMs.[34] They found that CAPE caused the frequency-dependent measurement amplitude distortion in the nuclear magnetic resonance (NMR) spectrum. Later, Borna et al. simulated and measured the sensitive axis rotation and amplitude error with CAPE and examined the impact of CAPE on the source localization capabilities of the OPM-MEG systems.[1] Recently, Lin et al. presented a detailed analysis of interaxial time-domain interference in a single-beam SERF magnetometer. The potential measurement error induced by interference was also demonstrated in an MCG simulation.[35] However, these studies did not consider measurement errors in the OPM gradiometer configuration. The measurement error analysis of magnetic gradiometers is not identical to that of a single magnetometer. Gradient measurement errors are related to not only the measurement errors of the individual magnetometers, but also the inconsistency of their properties and performance.

In this study, we first analyzed the interference-dependent gradient phase and amplitude errors which were highly dependent on the atomic relaxation rate differences and residual magnetic fields. Combined with theoretical analysis and physical model, we detailly demonstrated this frequency-dependent magneto-optical interaction with atoms and further explored the induced measurement error in MCG and MEG systems based on OPM gradiometers. Finally, we provided a discussion and conclusion regarding the significance of the gradient difference error and the calibration method in practical applications.

RESULTS

Dynamic response of the single-beam modulated atomic magnetometer

In general, an OPM system resembles a first-order low-pass filter, where the bandwidth f_b (3 dB point) is determined by the total relaxation rate Γ' of the atomic ensemble, giving by $f_b = \Gamma'/(2\pi q)$, with q represents the slowing down factor of ^{87}Rb. In a near-zero magnetic field environment, the amplitude spectrum $M(\omega_s, \Gamma')$ and phase spectrum $\varphi(\omega_s, \Gamma')$ of the OPM have the following form:

$$\begin{cases} M(\omega_s, \Gamma') = \dfrac{1}{\sqrt{1+\left(\dfrac{\omega_s q}{\Gamma'}\right)^2}} \\ \varphi(\omega_s, \Gamma') = -\arctan\left(\dfrac{\omega_s q}{\Gamma'}\right) \end{cases}, \quad \text{(Equation 1)}$$

where ω_s is the angular frequency of the external magnetic signal to be measured. Equation 1 shows that when the residual static magnetic field can be ignored, for a signal with a certain frequency, the response amplitude and phase delay of OPM are only related to Γ'. However, it is impossible to analytically solve the frequency response of the single-beam modulated OPM when a significant static magnetic field exists along the laser's propagation axis.[1] Comparing the steady-state solution of dual-beam OPMs[36] with the first harmonic steady-state solution of the single-beam modulated OPM,[37] we know that they have the same form as a function of pumping rate R_{op}, Γ', and the external magnetic field, except for the Bessel functions introduced by the high-frequency modulation field. Therefore, we can approximately derive the first harmonic dynamic response of the single-beam modulated OPM under non-negligible static magnetic field with the reference to the dual-beam configuration.[34] Since the magnetic field compensation along the pump axis (B_z) is the most error-prone and contributes the most to measurement errors,[1] we only consider the effect of the bias field B_z. Assuming that the angle between the external field $B_s\,cos(\omega_s t)$ to be measured and the sensitive axis (x-axis) is θ, the spin polarization along the pumping beam (P_z) can be expressed as:[35]

$$P_z(t) = 2J_0J_1\frac{R_{op}}{\Gamma'}\left[\Omega_s\cos\theta\frac{\sqrt{\Gamma'^2+\omega_s^2q^2}\cos(\omega_s t+\varphi_x)}{\sqrt{\left(\Gamma'^2-J_0^2\Omega_z^2+\omega_s^2q^2\right)^2+4\Gamma'^2J_0^2\Omega_z^2}}+J_0^2\Omega_s\sin\theta\frac{\Omega_z\cos\left(\omega_s t+\varphi_y\right)}{\sqrt{\left(\Gamma'^2-J_0^2\Omega_z^2+\omega_s^2q^2\right)^2+4\Gamma'^2J_0^2\Omega_z^2}}\right], \quad \text{(Equation 2)}$$

where $\Omega = \gamma B$ is the atomic Larmor precession rate in the external magnetic field B, $\varphi_x = \arctan\left(\frac{-\omega_s q(\Gamma'+\omega_s^2q^2-J_0^2\Omega_z^2)}{\Gamma'(\Gamma'^2+\omega_s^2q^2+J_0^2\Omega_z^2)}\right)$ and $\varphi_y = \arctan\left(\frac{-2\omega_s q\Gamma'}{\Gamma'^2-\omega_s^2q^2+J_0^2\Omega_z^2}\right)$. For simplify, we use J_n to represent $J_n(u)$, where J_n denotes the nth order Bessel functions of the first kind. See STAR Methods for the specific derivation process.

Definition of gradient phase and amplitude errors

The observation from Equation 2 is that in the condition of existing residual magnetic fields in pumping axis, the magnetic field along non-sensitive axis (y axis) will also generate response, introducing the response cross-talk between the two non-pumping axes in both amplitude and phase. Furthermore, the response phase of the OPM is determined by the total relaxation rate Γ'. Therefore, if the properties of the two channels in the gradiometer configuration are different, the response phase of which will also be different, even if B_z is zero.[13,26] The specific frequency characteristics of the response amplitude and phase to the external signals can be quantified, fitted, and analyzed according to Equation 2. Thus, we studied the performance of OPM gradiometers based on the above theory as the following two cases.

Case I (gradient phase error): $\theta = 0$: Although a single OPM does not experience the amplitude errors caused by φ_x, the existence of B_z and the difference in Γ' introduce a response phase difference between multiple OPMs, ultimately leading to measurement errors in multi-channel systems. In this paper, this measurement error is termed as the gradient phase error. The output signal of the OPM ($V(t) = A_0 P_z(t)$) is an oscillating signal, where A_0 represents the conversion factors of the photodetector and other system parameters. Hence, we can write the difference amplitude of the OPM gradiometer as:

$$V_{diff} = \sqrt{\left(V_{ax}{}^2 + V_{bx}{}^2 - 2V_{ax}V_{bx}\cos(\Delta\varphi)\right)}, \quad \text{(Equation 3)}$$

where $\Delta\varphi = \varphi_{ax} - \varphi_{bx}$, where φ_{ax} and φ_{bx} are the response phases of x-axis of the two OPMs. $\Delta\varphi$ is determined by the signal frequency, relaxation rate and z axis bias field. Equation 3 reveals that $\Delta\varphi$ distorts the output amplitude of the OPM gradiometer and further introduces measurement error. Even when B_z is small enough to be neglected, the gradient phase error exists if the relaxation rates of the two OPMs are different. The existence of the gradient phase error is not confined solely to the sensitive axis, but is also present in the non-sensitive axis. Nevertheless, in cases where the external magnetic field angle is small or the y axis response is inferior to that of the x-axis, the contribution of the gradient phase error from the non-sensitive y axis to the total error is negligible. In this study, we mainly consider a special case where θ is equal to $\pi/2$, such as the maternal cardiomagnetic signal at the sensor position during fMCG measurement. Generally, the gradient difference technique is employed to suppress the maternal signal; however, the difference in φ_y degrades the accuracy of the common mode noise suppression.

Case II (gradient amplitude error): $\theta \neq 0$: The presence of B_z causes P_z also sensitive to the magnetic field along the y axis and thus rotates the sensitive axis. When the external magnetic field is not parallel to the x-axis, the actual output amplitude of a single OPM in the gradient configuration can be expressed by:

$$V_i = \sqrt{\left(V_{ix}{}^2 + V_{iy}{}^2 + 2V_{ix}V_{iy}\cos(\Delta\varphi)\right)}, \quad \text{(Equation 4)}$$

where $i = a, b$, $\Delta\varphi = \varphi_{ix} - \varphi_{iy} = \arctan(\omega_s q/\Gamma')$. $\Delta\varphi$ is the inherent response phase difference between the two non-pumping axes. V_i combines the responses of the two non-pumping axis fields, leading to measurement errors. In addition, different OPMs in the gradient configuration have diverse response characteristics, inducing different response proportions of x axis and y axis. Previous studies have systematically discussed the deterministic measurement error that arises from the interaxial response interference of a single-beam modulated SERF magnetometer.[35] In this study, we focus on the measurement error arising from the collective effect of the magnitude distortion exhibited in each OPM in the gradient configuration, which is referred to as the gradient amplitude error. Note that $\Delta\varphi$ is only related to the frequency of the external magnetic field and the relaxation rate of the atomic ensemble. However, Equation 2 shows that alterations in V_i are associated with the angle between the external field and x-axis. It is apparent that, given a constant residual magnetic field, an increase in the angle between the external field and the x-axis corresponds to an increase in the degree of y axis response. This leads to an increase in the resulting error. This is particularly important in MEG and MCG applications where the signals of interest may not be entirely parallel to the sensitive axis.

Calculation of gradient phase and amplitude errors

Calculation of the gradient phase error: Differences in relaxation rate and residual magnetic fields cause OPMs to exhibit distinct response phases to a dynamic magnetic field. To evaluate the gradient error resulting from the different response phases of OPMs, a set of coils embedded in the magnetic shield was used to apply a 100 pTrms sinusoidal magnetic field along the sensitive axis of the gradiometer. Each OPM's output was continuously collected for 100 s and subsequently normalized. The normalized dynamic outputs of the two OPMs were directly subtracted. The difference signal was then processed through transformation and calculation using fast Fourier transform (FFT) to determine the effective value of the component at the same frequency as the applied signal. This value was used to quantify the magnitude of the gradient phase error. When the response phases of the two OPMs were identical, the theoretical difference result was zero.

Calculation of the gradient amplitude error: B_z induces the OPM to respond to the magnetic field along the non-sensitive axis, causing a rotation of the sensitive axis. To assess the gradient amplitude error caused by the rotation of the sensitive axis, a static field was applied along the z axis of one OPM of the gradiometer by a rectangular Helmholtz coil set surrounding each channel. The field produced by this coil was negligible at the position of the other channel. Additionally, a 100 pTrms sinusoidal magnetic field was applied by a set of shield coils along the direction at an angle θ with x-axis (in x-y plane). The dynamic responses of the two OPMs were collected for 100 s and subjected to FFT to obtain the response amplitudes. Note that the OPM response amplitude at $\theta = 0$ is typically used as a scale factor for converting the OPM response amplitude to the magnetic field amplitude. Utilizing this scale factor, the OPM response amplitudes at different θ were normalized. The normalized response amplitudes of the two OPMs were differenced to characterize the magnitudes of the gradient amplitude error. The theoretical difference result was expected to be zero when $B_z = 0$ (no sensitive axis rotation).

Experimental setup

Our experimental measurement based on our self-designed compact four-channel OPM sensor with high spatial resolution, similar to the work reported in,[38] as shown in Figure 1A. The sensor has a compact volume of only 18 cm^3. It can be served as four separate atomic magnetometers or as two synthetic gradiometers formed by two adjacent channels. The experimental apparatus depicted in

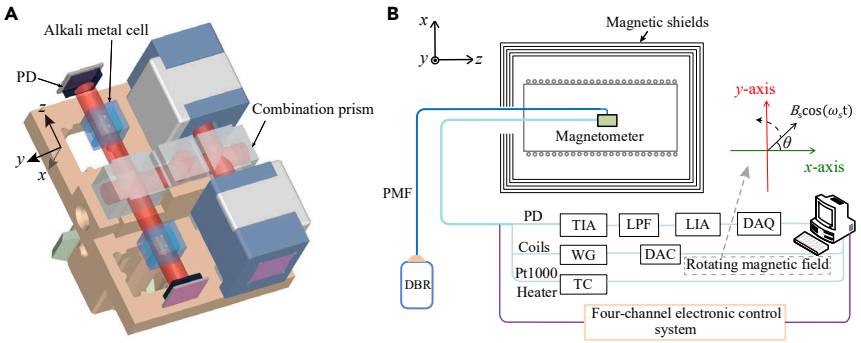

Figure 1. The structure of the OPM sensor and the experimental setup

(A) The multi-channel OPM sensor's schematic. The sensor has a total volume of about 18 cm^3. Each vapor cell contains 600 Torr N_2 in addition to a small amount of ^{87}Rb metal. PD: photodetector.

(B) The experimental setup based on single-beam principle. DBR: distributed Bragg reflector. PMF: polarization-maintaining fiber. TIA: transimpedance amplifier. LPF: low-pass filter. LIA: lock-in amplifier. DAQ: data acquisition. WG: waveform generator. DAC: digital-to-analog converter. TC: temperature controller.

Figure 1B was employed to provide magnetic signals and record the response of the OPM. See STAR Methods for details of experimental operation.

Simulation of gradient phase error

Simulation calculations were performed to assess the gradient phase error with the assumption that the same calibration signal was applied to the two OPMs in the gradiometer configuration. Figure 2 provides an overview of how the gradient phase error varies as a function of signal frequency under different residual magnetic fields (B_z) and bandwidth divergences. Figure 2A depicts the correlation between the gradient phase error and signal frequency at $\theta = 0$, which is notably impacted by the differences between channels. Figure 2B displays the computed gradient phase error when measuring the signal along the non-sensitive y axis ($\theta = \pi/2$) for comparison with Figure 2A. Figure 2B follows a similar trend to Figure 2A, with the gradient phase error of the non-sensitive axis significantly larger than that of the sensitive axis. The observation from Figure 2 demonstrates a considerable increase in the measurement error of the OPM gradiometers as the bandwidth decreases, particularly in the low-frequency range. This indicates that the gradient measurement error has a greater impact on measurement systems utilizing OPM sensors with narrower bandwidths. It's worth noting that in the simulations sections, both the gradient phase and amplitude errors represent the proportion of the differential result to the amplitude of the original calibration signal.

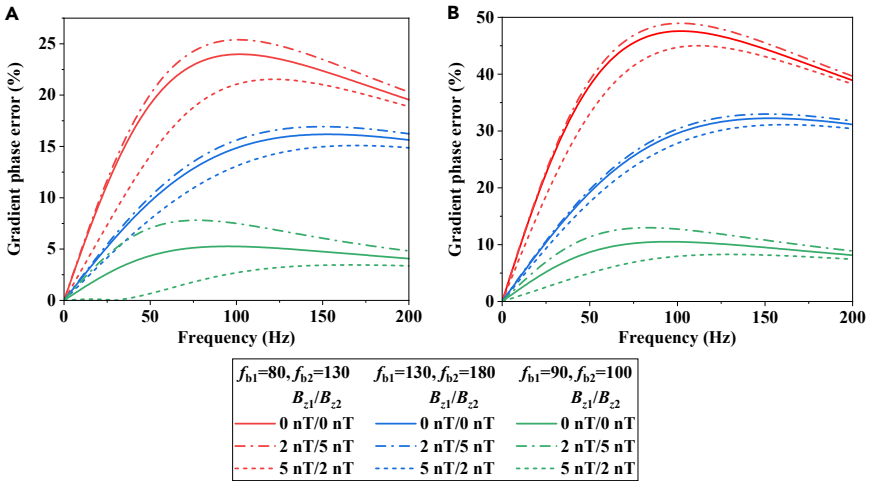

Figure 2. The calculated gradient phase error varies with the signal frequency under different B_z and bandwidth differences

The simulated gradient phase error represents the proportion of the differential result to the amplitude of the original calibration signal.

(A) The measured signal along the x-axis ($\theta = 0$).

(B) The measured signal along the y axis ($\theta = \pi/2$).

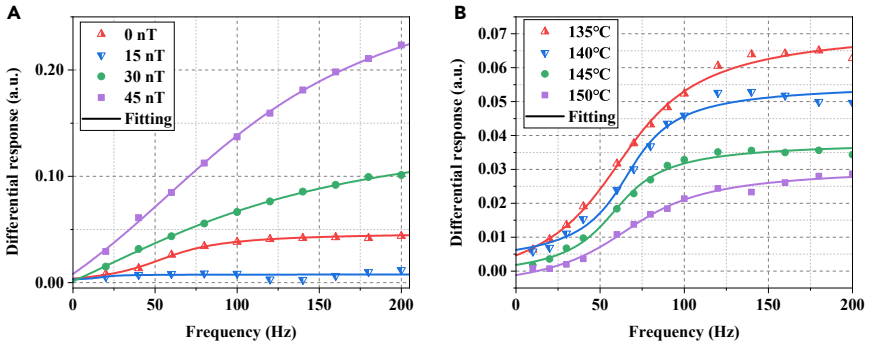

Figure 3. The measured amplitude error of the OPM gradiometer caused by the gradient phase error as a function of signal frequency

In order to eliminate the error caused by the fluctuation of the scale factor, the output of each OPM is normalized.

(A) The measured amplitude error at different B_z.

(B) The measured amplitude error at different cell temperatures.

Experimental measurement results of gradient phase error

Figure 3 illustrates that the gradient phase error affects the non-sensitive axis more significantly. Therefore, we focused on evaluating the effect of the gradient phase error on the suppression performance of OPM gradiometers for the *y* axis response. This is critical when gradiometers are used to eliminate common-mode background signals along the *y* axis, as in the case of the maternal cardiomagnetic signal during fMCG measurement.

Two arbitrary channels in the four-channel magnetometer shown in Figure 1A were selected to form a synthetic gradiometer. The four-channel electronic control system illustrated in Figure 1B ensured that the two OPMs operated simultaneously. A uniform field was applied along the non-sensitive at the sensors position. Under ideal conditions, the gradiometer output should be zero. However, with the similar trend with the simulation results, the difference of the two OPMs was nonzero and increased with the signal frequency as shown in Figure 3. Thus, we demonstrate that the gradient phase error is dominant in the high frequency band. Then, the magnetic field of 15 nT was applied above the B_z magnetic compensation zero point of one channel in the gradiometer configuration, and we found that the differential result was approximately zero, as shown by the blue line in Figure 3A. We demonstrate that introducing an extra magnetic field to one channel diminishes the phase difference in response between the two magnetometers, resulting in a reduction in the gradient phase error; however, if B_z continues to increase on this basis, the gradient phase error will increase significantly. To assess the impact of bandwidth differences between channels on the gradient phase error, the temperatures of both channels were simultaneously adjusted, as depicted in Figure 3B. A modest increase in the temperature in both channels leads to a reduction of the gradient phase error. Such decrease is attributed to a reduction in the bandwidth difference between channels, aligning with the trend observed in the simulated influence of bandwidth difference on the gradient phase error in Figure 2. It is worth mentioned that because of the relatively low accuracy of the automatic magnetic compensation algorithm of the four-channel electronic control system, the magnetic compensation point (0 nT) in this section does not truly represent the point at which B_z equals to zero.

Furthermore, we analyzed the impact of the gradient phase error on the measurement accuracy of an fMCG system. In the actual measurement, the maternal heart was located farther away from the magnetometer than the heart of the fetus, and the direction of maternal cardiac magnetic field was nearly perpendicular to the sensitive axis of the sensor. Consequently, the maternal heart magnetic signal was considered as a more uniform background field than the fMCG signal. Thus, the gradient differential method can be used to partly suppress the maternal heart magnetic signal in the fMCG measurement system.[39] A shield coil set, driven by a waveform generator, provided a simulated uniform cardiac magnetic field with a frequency of 1 Hz and an effective value of 100 pT in the non-sensitive axis direction. The output of the OPM gradiometer was then calculated under several different static magnetic fields along the pump laser propagation axis. In Figure 4, the power spectral density (PSD) is presented for both the single-channel cardiac magnetic field signal and the differential signal obtained from the two OPMs. The cardiomagnetic signal primarily falls within the frequency range of 50 Hz, as indicated by the black line in Figure 4. The presence of B_z leads to the excitation of the OPMs' response to the magnetic field along the *y* axis. Moreover, because of the difficulty in maintaining consistent relaxation rates among the OPMs, the phase error is introduced, causing the noise suppression ability of the OPM gradiometer to reduce. Although the gradient phase error is more significant in high frequency band, we note that with increasing B_z, the impact of the error on relatively low-frequency MCG signals cannot be ignored.

To eliminate the gradient phase error, merely compensating B_z to zero is insufficient. Figure 2 shows that the gradient phase error persists even when $B_z = 0$ if there is a bandwidth difference between the OPMs. Therefore, in gradiometer applications, it is necessary to reduce the relaxation difference between channels without compromising the OPMs' fundamental performance by adjusting parameters such as B_z, pumping light intensity and cell temperature to minimize the gradient phase error. Afterward, relatively high-frequency signals can be applied to confirm the efficacy of error suppression.

Simulation of gradient amplitude error

Simulation calculations were conducted to evaluate the gradient amplitude error, assuming that an identical calibration signal was applied to both OPMs in the gradiometer configuration. The static magnetic field present along the pumping axis excites the OPM response to the

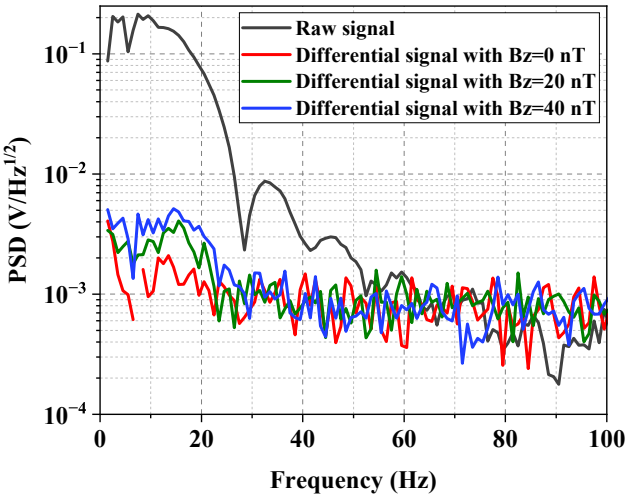

Figure 4. The influence of B_z on the suppression performance of OPM gradiometers for the simulated maternal cardiomagnetic signals along non-sensitive axis (*y* axis) in the fMCG measurement

magnetic field aligned with the non-sensitive axis, which eventually induces the gradient amplitude error. The relationship between the calculated amplitude error and signal frequency at different θ is depicted in Figure 5. When the remanence of the pumping axis is null, the amplitude error becomes zero. However, when the remanence is nonzero, the amplitude error increases with the differences between the channels. Notably, a larger θ leads to a more substantial error. This is particularly important in MEG and MCG applications where the signals of interest may not be entirely parallel to the sensitive axis. Upon comparing Figures 2 and 5, it becomes evident that the variation in bandwidth between channels has a greater impact on the gradient phase error, whereas the difference in static magnetic field along the pumping axis between channels notably influences the gradient amplitude error. In general, both the gradient phase and amplitude errors decrease as the performance difference between channels narrows. Figures S1 and S2 represent additional simulation results of gradient phase and amplitude errors with higher B_z difference and smaller bandwidth difference.

Experimental measurement results of gradient amplitude error

The response of the OPM to the magnetic field along the non-sensitive axis is visually illustrated by the rotation of the sensitive axis. To quantify the correlation between the rotation angle of the sensitive axis and the static magnetic field along the pumping axis, a sinusoidal field with

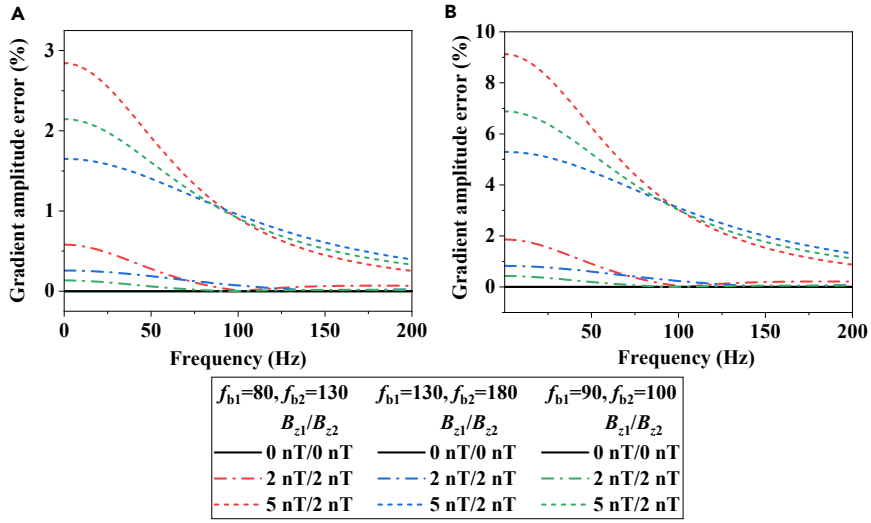

Figure 5. The calculated gradient amplitude error varies with the signal frequency under different B_z and bandwidth differences

The simulated gradient amplitude error represents the proportion of the differential result to the amplitude of the original calibration signal.

(A) θ = 0.15 rad.

(B) θ = 0.5 rad.

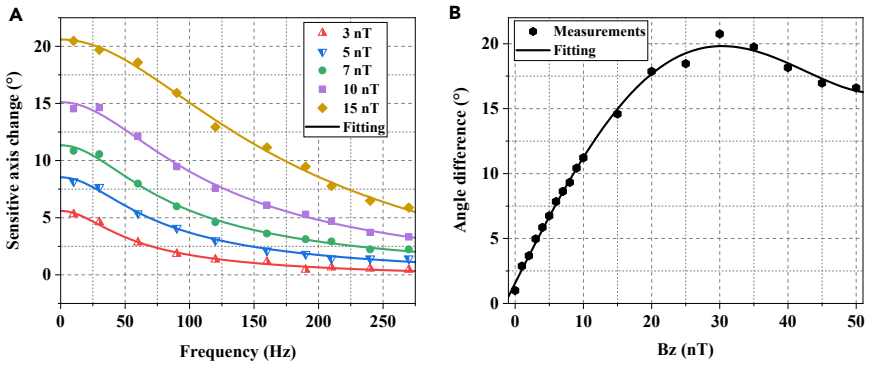

Figure 6. Experimental observation regarding the rotation of the sensitive axis

(A) Relationship between the sensitive axis rotation and the signal frequency under different static magnetic fields.

(B) The difference between the rotation angle of the sensitive axis at 10 Hz and 270 Hz under different static magnetic fields.

a frequency range of 10–270 Hz and an effective value of 100 pTrms was generated using shield coils driven by a digital-to-analog converter. The applied rotating field, with a resolution of 0.1°, was rotated in the *x-y* plane. This experiment was conducted on a single OPM. Figure 6A demonstrates a notable correlation between the sensitive axis rotation angle with the signal frequency and B_z. As $\Delta\varphi$ varies with the signal frequency, the response coupling between the two non-pumping axes is frequency-dependent. This coupling is dominated by low-frequency signals, aligning with the correlation between gradient amplitude error and signal frequency observed in Figure 5. Meanwhile, the rotation angle of the sensitive axis increases with the increase in B_z. Additionally, the rate at which the rotation angle decreases with frequency increases with larger B_z values, suggesting a widening gap between the rotation angles at low and high frequencies. However, this relationship is not linear, as illustrated in Figure 6B. Specifically, the disparity between the low and high frequencies first increases and then decreases as B_z increases. This is attributed to the fact that while increasing B_z enhances the response of the non-sensitive axis, it also affects the bandwidth and scale factor of the OPM system.

When the signal aligns with the sensitive *x*-axis, the calibration process can prevent amplitude measurement errors resulting from the rotation of the sensitive axis. However, the limitations of practical conditions often result in the signal being at an angle relative to the *x*-axis. According to Equation 4, when the external magnetic field is not parallel to the *x*-axis, the collective amplitude distortion exhibited by each OPM in the gradient configuration causes the gradient amplitude error to emerge. The normalized response amplitudes of the two OPMs at various frequencies and incident angles of the external magnetic field are shown in Figures 7A and 7B, respectively, and their differential amplitudes are depicted in Figure 7C. Each OPM' response amplitude was obtained by applying a 10 nT remanence to their pumping axes after the magnetic field was compensated.

As shown in Figures 7A and 7B, the OPM response is affected by the sensitive axis rotation, resulting in an initial increase and subsequent decrease in the response as θ increases. Although different OPMs exhibits varying response trends with parameter changes, the overall relationship holds true. The findings confirm that the rotation of the sensitive axis causes a greater amplitude distortion of the OPM for low-frequency signals, consistent with the experimental results presented in Figure 6A. The data presented in Figure 7C further support this conclusion, as the figure depicts a decrease in the gradient error as the signal frequency increases, which is in a good agreement with the simulation results presented in Figure 5. The black line in Figure 5 indicates that the gradient amplitude error can be eliminated when the value of B_z is zero. A widely used method to compensate for the residual static magnetic field is to ensure that the dispersion curve of the sensitive *x*-axis response crosses the zero point. However, it should be noted that the zero crossing of the dispersion curve does not necessarily indicate that the response of the non-sensitive *y* axis is zero. Hence, we propose our precise magnetic field compensation method. First, using the conventional single-beam OPM magnetic compensation method[40] to offset the triaxial remanence, ensuring the dispersion curve of the sensitive-axis response intersects the zero point. Subsequently, minimize the response of the non-sensitive axis by adjusting B_z, as illustrated in Figure 8A. Following this, compensate *x* and *y* axis remanence again to eliminate the effect of the coils' orthogonal angle. Finally, the scale factor of the response of the *x*-axis will increase accordingly, as shown in Figure 8B. Using our method, the scale factor of the *y* axis can be decreased by 86%, while the scale factor of the sensitive *x*-axis can be further increased by 4%.

Impacts of gradient phase and amplitude errors on the localization accuracy of OPM-MEG systems

An OPM-MEG simulation was conducted to evaluate the effects of the gradient errors on the localization accuracy of the MEG system. The simulation and processing tasks for the MEG signals were based on FieldTrip, an open-source MATLAB toolbox for advanced MEG analysis.[41] A 20-channel OPM-MEG system consisting of five four-channel magnetometers, as shown in Figure 1A, was simulated. The channel positions were artificially adjusted to approximately cover the auditory cortex of the right brain, as shown in Figure 9. The single-shell model developed by Nolte was used as the head-volume conduction model. Following the auditory oddball experiment provided by the NatMEG workshop, the position and orientation of the activated cortex were determined using the equivalent current dipole model. First, we used the forward modeling method to determine the magnetic field distribution induced by the calculated activated source at all the channel location. The

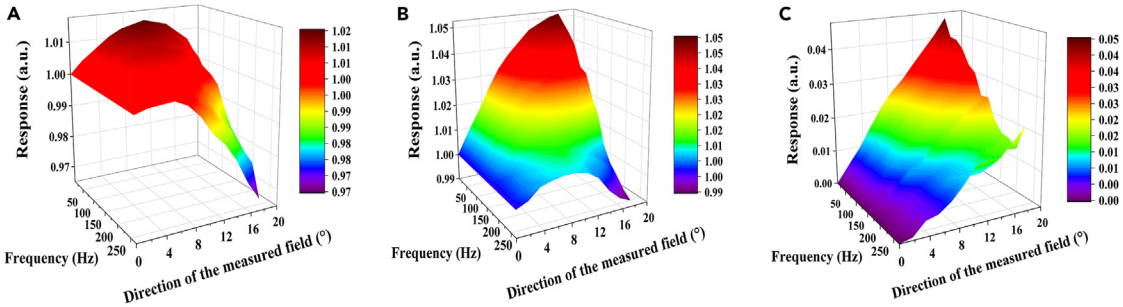

Figure 7. The experimental results of the gradient amplitude error

(A) The normalized responses of channel 1 at different frequencies and incident angles (θ) of the external magnetic field.

(B) The normalized responses of channel 2 at different frequencies and incident angles (θ) of the external magnetic field.

(C) The amplitude difference between the two OPMs.

ideal OPM output was then modified by calculating the output affected by the gradient errors in the presence of a static magnetic field on the laser's propagation axis, according to the previously discussed theory. Finally, the dipole fitting method provided by Fieldtrip was used again to estimate the new source location corresponding to the calculated outputs of all channels.

The OPM-MEG system is typically located in a magnetic shielding room and experiences a non-uniform gradient magnetic field. Owing to limitations in the accuracy of the magnetic compensation system and the residual fictitious magnetic field resulting from the intensity and frequency fluctuations of the pumping light, it is difficult to eliminate the gradient phase and amplitude errors, which have a negative impact on the localization capability of the OPM-MEG system, particularly for wearable systems that require displacement. Furthermore, the errors are highly dependent on signal frequency, which places higher demands on the pre-use calibration process of OPM-MEG, as the brain source signals picked up by the MEG system cover a wide frequency range of 10–100 Hz.[42] In this section, we discuss the errors in source location for OPM-MEG gradient measurement systems with varying performance when exposed to a random residual DC magnetic field and different frequency signals. To simulate a random B_z scenario, each OPM channel was assigned a random static magnetic field along the laser propagation axis. The field was drawn from a normal Gaussian distribution with different means (μ) and standard deviations (σ). Random distributions were generated 20 times, and the results were averaged.

The effect of the gradient phase error on the OPM-MEG source localization system was first analyzed, assuming that the angle between the direction of the signal to be measured and the *x*-axis was negligible. Figure 10 displays the average values of the source localization error for different frequency signals when changing the standard deviation of B_z ($\sigma((B_z))$) at different B_z mean values ($\mu(B_z)$). The mean values of B_z in Figures 10A and 10B are 5 and 10 nT, respectively. Each pair of OPMs that constituted the gradiometer possessed bandwidth of 80 and 130 Hz. The source localization error increases with the mean and standard deviation of B_z, indicating that the greater the difference in the residual magnetic field between the channels, the larger the localization error. The relationship between the source localization error and signal frequency exhibits the same trend as the simulation results in Figure 2 and the measured results in Figure 3. In comparing Figures 10A and 10B, we find that as $\mu(B_z)$ increases, the maximum error point moves toward higher frequencies. For a $\mu(B_z)$ of 10 nT and a $\sigma(B_z)$ of 5 nT, the induced average source localization error can be greater than 1 cm for signals with frequencies of about 100 Hz. To quantify the effect of the channel bandwidth on the localization error, the bandwidth values of each pair of OPMs were increased to 130 Hz and 180 Hz and the experiments described above

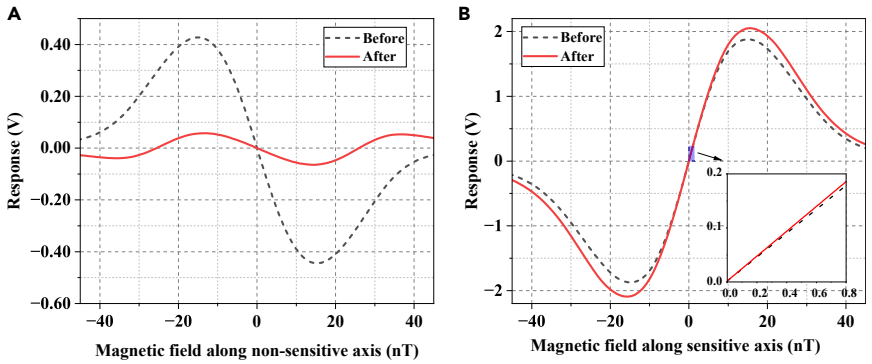

Figure 8. The OPM responses with respect to the magnetic fields along two non-pumping axes

(A) The OPM response to the field along the *y* axis.

(B) The OPM response to the field along the *x*-axis. The inset of the range of the blue frame shows the comparison of the response scale factors of the sensitive axis with fully compensated B_z and with incompletely compensated B_z in the linear region.

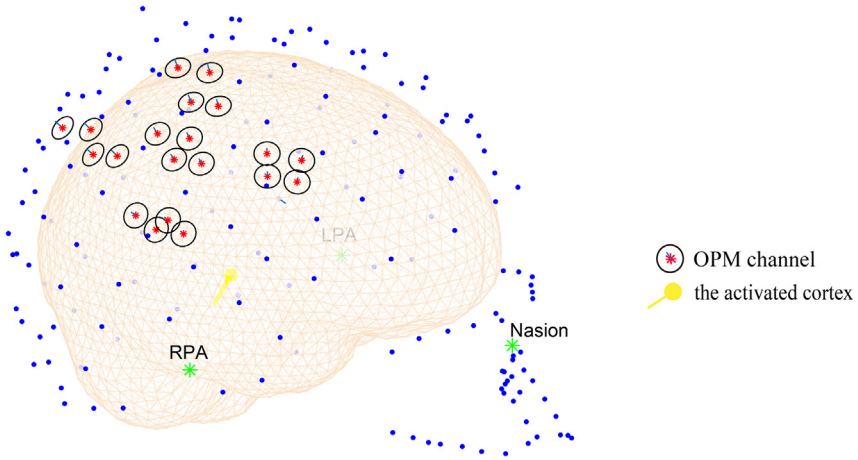

Figure 9. The simulated 20-channel OPM-MEG system

The OPM array covers the auditory cortex of the right brain. The blue dots represent the head shape, while the skin-colored grids depict the head model. Each channel's position is marked by a black circle, and the center of each channel is indicated by a red dot. The yellow round arrow represents the activated cortex. The LPA point corresponds to the left pre-auricular, and the RPA point corresponds to the right pre-auricular.

were repeated (see Figure S3). Based on the above simulations, we conclude that the impact of the gradient phase error is more significant on the MEG system using OPMs with narrower bandwidth.

When the external magnetic field is not strictly parallel to the sensitive axis, the presence of the static magnetic field along the laser propagation direction causes interaxial response interference. Equation 2 shows that the distortion of the OPM output is associated with the angle between the external field and the sensitive x axis (θ). An increase in θ corresponds to an increase in the non-sensitive axis response under a certain B_z. Figure 11 illustrates the average values of the simulated source localization error induced by the gradient amplitude error for different frequency signals when changing the standard deviation of B_z at different incident angles of the measured signals. Unlike the localization error induced by the gradient phase error, the localization error induced by the gradient amplitude error decreases as the frequency increases. Additionally, it has been verified that the error increases with larger θ, consistent with the simulation results shown in Figure 5 and the measured results in Figure 7. Similar to the abovementioned simulation process of the gradient phase error, we also increased the OPM bandwidth and repeated the simulation process (see Figure S4). In the MEG system constructed using OPMs with a narrower bandwidth, the gradient amplitude error diminishes more rapidly with increasing frequency.

Consequently, the gradient phase and amplitude errors simultaneously induce source location errors. From Figures 10 and 11, we can infer that the location error can accumulate to over 2 cm, which severely reduces the accuracy of MEG or MCG systems. In practical gradient applications, the gradient errors should be considered and compensated for.

DISCUSSION

In recent years, the CAPE in OPMs has garnered widespread attention among researchers due to its crucial significance in optimizing OPM performance. In this study, we presented a comprehensive theoretical and experimental analysis of the gradient phase and amplitude errors in a single-beam modulated SERF atomic magnetic gradiometer. Specifically, we examined the relationship between the errors and signal frequency, angle of the external magnetic field, and performance consistency between channels. The simulation results agree well with the experimental data. For practical applications, we employed simulations to assess the impact of the errors on OPM gradiometer-based MEG and MCG systems. Our results reveal that the effect of the errors is non-negligible in high-precision biomagnetic measurement systems that use OPM gradiometers. In addition to the impact on synthetic gradiometer approaches, the gradient phase and amplitude errors will also influence the accuracy of the source inversion algorithm. For instance, the different response phases of OPMs may result in the temporal accuracy reduction of the inversion algorithm.[43,44] Due to the different frequency characteristics of the gradient errors, researchers need to focus on different priorities when selecting source inversion systems for diagnosing different diseases under different frequency bands.

Because the gradient phase and amplitude errors are inherent error terms in gradient measurements through atomic ensembles, our investigation delves beyond single-beam OPM gradiometers. The response of the OPM system to an external magnetic field resembles that of a low-pass filter, exhibiting a frequency response similar to that of the conventional filter. Each OPM exhibits an intrinsic phase delay in its response to an external magnetic field, which is primarily related to the relaxation of the atomic ensemble, residual field, and signal frequency. When the external magnetic field is aligned with the sensitive axis, the response phase difference of each single OPM introduces a zero-crossing error in the multichannel OPM measurement system, which can be readily detected by visual inspection. However, for gradiometer configurations, the variation in the response phase among OPMs yields the emergence of the gradient phase error, distorting not only the phase delay of a single OPM but also the amplitude of the gradiometer output. In addition, the gradient phase error shows the frequency-dependent characteristic that dominants in high-frequency band, which fits our theory well. Notably, compensating B_z to zero fails to eliminate

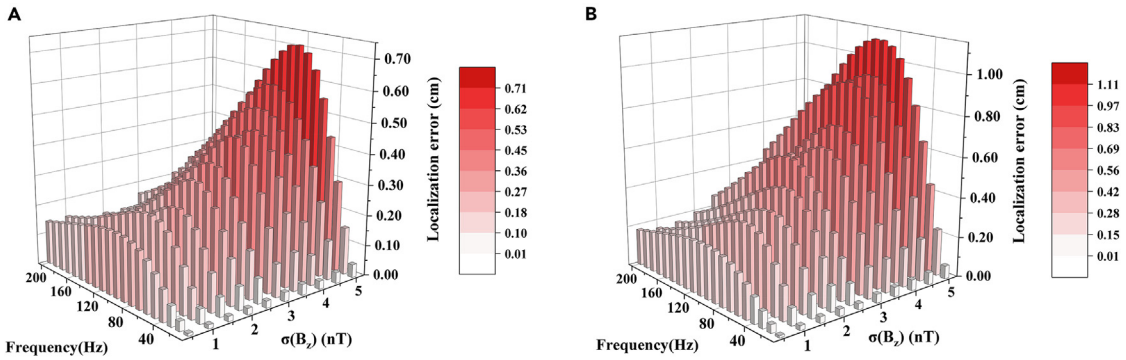

Figure 10. The simulated source localization error induced by the gradient phase error at various signal frequencies and standard deviations of residual static magnetic fields on pumping axis

The bandwidths of the two OPMs that constitute the gradiometer are 80 Hz and 130 Hz, respectively.

(A) $\mu(B_z)$ = 5 nT.

(B) $\mu(B_z)$ = 10 nT.

the impact of the gradient phase error, given its greater susceptibility to relaxation consistency between channels. Thus, when constructing an OPM gradiometer, pre-calibration of the OPM bandwidth and reduction in their difference are crucial and can be achieved by manipulating the operating temperature of the alkali metal cell and adjusting the pumping light intensity. However, in practical applications, an ideal alignment between the external magnetic field and the sensitive axis of the OPM is often unattainable. The presence of B_z causes rotation of the sensitive axis, thus compromising the calibration of the OPM and resulting in amplitude errors. When multiple OPMs are combined in a gradient configuration, the amplitude distortion of a single OPM is amplified, resulting in the gradient amplitude error. The gradient amplitude error shows the frequency-dependent characteristics that dominants in low-frequency band. Meanwhile, the impact of B_z can be mitigated by compensating it to zero. Therefore, the effective elimination of residual magnetic fields in the magnetic shielding room is crucial to ensure the accuracy of OPM measurements. In general, correlated variations in B_z depict a more realistic scenario where environmental fluctuations induce similar changes among OPMs, leading to comparatively minor errors. However, when OPMs are allowed to move in the remnant background field, the uncorrelated changes of B_z will generate more problematic gradient phase and amplitude errors.[33] Thus, the accuracy and consistency of the active magnetic field zeroing technique become more significant. We believe that the ongoing development of calibration and real-time residual magnetic field zeroing techniques holds promise for reducing the effects of these inherent gradient errors on OPM gradiometers, thereby realizing the advantages of OPM gradiometer-based biomagnetic measurement systems.

Limitations of the study

We configured 20 fixed-location channels in the simulated OPM-MEG system. However, to enhance the measurement sensitivity and spatial resolution, the latest OPM-MEG systems now have involved hundreds of channels. Therefore, our simulation settings may also be improved synchronously to simulate the most realistic testing conditions.

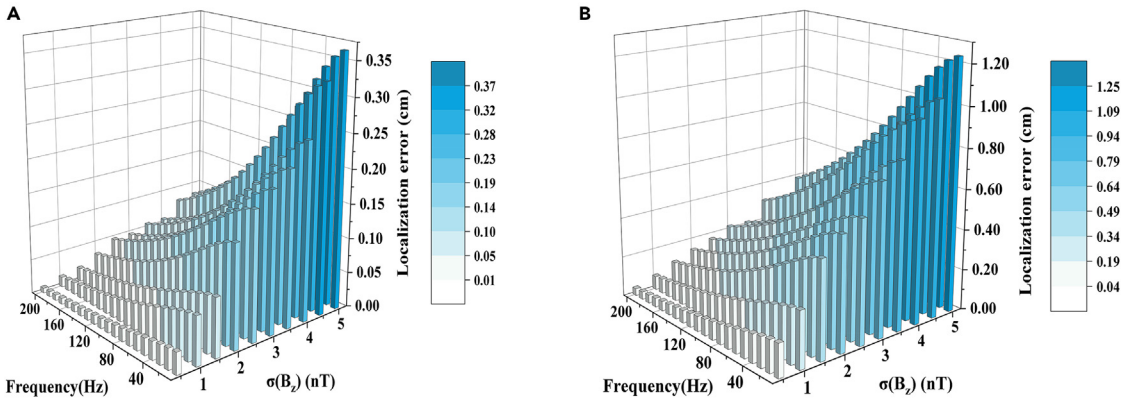

Figure 11. The simulated source localization error induced by the gradient amplitude error at various signal frequencies and standard deviations of residual static magnetic fields with $\mu(B_z)$ = 5 nT

The bandwidths of the two OPMs that constitute the gradiometer are 80 Hz and 130 Hz, respectively.

(A) θ = 0.03 rad (1.72 °).

(B) θ = 0.15 rad (8.60 °).

In addition, we have preliminarily validated the effective suppression of gradient difference errors through magnetic field closed-loop control (not shown in this paper). Nevertheless, this approach will introduce additional noises and other measurement errors. In the future, we will further investigate the impact of closed-loop control on the performance of the gradient measurement system to improve the reliability of the OPM gradient measurement system.

STAR★METHODS

Detailed methods are provided in the online version of this paper and include the following:

- KEY RESOURCES TABLE
- RESOURCE AVAILABILITY
  - Lead contact
  - Materials availability
  - Data and code availability
- EXPERIMENTAL MODEL AND STUDY PARTICIPANT DETAILS
- METHOD DETAILS
  - Steady-state response of the dual-beam and single-beam modulated atomic magnetometer
  - Dynamic response of the dual-beam atomic magnetometer
  - Dynamic response of the single-beam modulated atomic magnetometer
  - Sensor structure
  - Experimental apparatus
- QUANTIFICATION AND STATISTICAL ANALYSIS

SUPPLEMENTAL INFORMATION

Supplemental information can be found online at https://doi.org/10.1016/j.isci.2024.109250.

ACKNOWLEDGMENTS

This work was supported by the National Natural Science Foundation of China (grant number 62003020), and the Innovation Program for Quantum Science and Technology (grant number 2021ZD0300500/2021ZD0300503).

AUTHOR CONTRIBUTIONS

Conceptualization, Z.Q.Y. and S.D.L.; Methodology, Z.Q.Y. and S.D.L.; Software, Z.Q.Y. and T.Y.L.; Formal analysis. Z.Q.Y. and S.D.L.; Resources, Y.L. and J.J.T.; Data curation, Z.Q.Y., S.D.L., Y.L., J.J.T., and Y.Y.Z.; Supervision, Y.L.; Project administration, Y.Y.Z.; Writing – original draft, Z.Q.Y.; Writing – review and editing, S.D.L., Y.L., J.J.T., and Y.Y.Z.

DECLARATION OF INTERESTS

The authors declare that they have no competing interests.

Received: November 28, 2023
Revised: January 30, 2024
Accepted: February 13, 2024
Published: February 16, 2024

REFERENCES

1. Borna, A., Iivanainen, J., Carter, T.R., McKay, J., Taulu, S., Stephen, J., and Schwindt, P.D.D. (2022). Cross-Axis projection error in optically pumped magnetometers and its implication for magnetoencephalography systems. Neuroimage *247*, 118818. https://doi.org/10.1016/j.neuroimage.2021.118818.
2. Koch, H. (2001). SQUID magnetocardiography: Status and perspectives. IEEE Trans. Appl. Supercond. *11*, 49–59. https://doi.org/10.1109/77.919284.
3. Kwong, J.S.W., Leithäuser, B., Park, J.W., and Yu, C.M. (2013). Diagnostic value of magnetocardiography in coronary artery disease and cardiac arrhythmias: A review of clinical data. Int. J. Cardiol. *167*, 1835–1842. https://doi.org/10.1016/j.ijcard.2012.12.056.
4. Kähkönen, S. (2006). Magnetoencephalography (MEG): a non-invasive tool for studying cortical effects in psychopharmacology. Int. J. Neuropsychoph. *9*, 367–372. https://doi.org/10.1017/S1461145705005894.
5. Hashimoto, H., Hasegawa, Y., Arak, T., Sugata, H., Yanagisawa, T., Yorifuji, S., and Hirata, M. (2017). Non-invasive detection of language-related prefrontal high gamma band activity with beamforming MEG. Sci. Rep. *7*, 1–8. https://doi.org/10.1038/s41598-017-14452-3.
6. Schneiderman, J.F. (2014). Information content with low-vs. high-Tc SQUID arrays in MEG recordings: The case for high-Tc SQUID-based MEG. J. Neurosci. Methods *222*, 42–46. https://doi.org/10.1016/j.jneumeth.2013.10.007.
7. Escalona-Vargas, D., Bolin, E.H., Lowery, C.L., Siegel, E.R., and Eswaran, H. (2020). Recording and quantifying fetal magnetocardiography signals using a flexible array of optically-pumped magnetometers. Physiol. Meas. *41*, 125003. https://doi.org/10.1088/1361-6579/abc353.
8. Brookes, M.J., Leggett, J., Rea, M., Hill, R.M., Holmes, N., Boto, E., and Bowtell, R. (2022). Magnetoencephalography with optically

pumped magnetometers (OPM-MEG): the next generation of functional neuroimaging. Trends Neurosci. *45*, 621–634. https://doi.org/10.1016/j.tins.2022.05.008.

9. Kim, K., Lee, W.K., Kim, I.S., and Moon, H.S. (2007). Atomic vector gradiometer system using cesium vapor cells for magnetocardiography: Perspective on practical application. IEEE Trans. Instrum. Meas. *56*, 458–462. https://doi.org/10.1109/tim.2007.890610.
10. Seymour, R.A., Alexander, N., Mellor, S., O'Neill, G.C., Tierney, T.M., Barnes, G.R., and Maguire, E.A. (2022). Interference suppression techniques for OPM-based MEG: Opportunities and challenges. Neuroimage *247*, 118834. https://doi.org/10.1016/j.neuroimage.2021.118834.
11. Vrba, J., and Robinson, S.E. (2002). SQUID sensor array configurations for magnetoencephalography applications. Supercond. Sci. Technol. *15*, R51–R89. https://doi.org/10.1088/0953-2048/15/9/201.
12. Nardelli, N.V., Perry, A.R., Krzyzewski, S.P., and Knappe, S.A. (2020). A conformal array of microfabricated optically-pumped first-order gradiometers for magnetoencephalography. EPJ Quant. Technol. *7*, 11. https://doi.org/10.1140/epjqt/s40507-020-00086-4.
13. Sheng, D., Perry, A.R., Krzyzewski, S.P., Geller, S., Kitching, J., and Knappe, S. (2017). A microfabricated optically-pumped magnetic gradiometer. Appl. Phys. Lett. *110*, 031106. https://doi.org/10.1063/1.4974349.
14. Boto, E., Meyer, S.S., Shah, V., Alem, O., Knappe, S., Kruger, P., Fromhold, T.M., Lim, M., Glover, P.M., Morris, P.G., et al. (2017). A new generation of magnetoencephalography: Room temperature measurements using optically-pumped magnetometers. Neuroimage *149*, 404–414. https://doi.org/10.1016/j.neuroimage.2017.01.034.
15. Boto, E., Seedat, Z.A., Holmes, N., Leggett, J., Hill, R.M., Roberts, G., Shah, V., Fromhold, T.M., Mullinger, K.J., Tierney, T.M., et al. (2019). Wearable neuroimaging: Combining and contrasting magnetoencephalography and electroencephalography. Neuroimage *201*, 116099. https://doi.org/10.1016/j.neuroimage.2019.116099.
16. Storm, J.H., Hömmen, P., Drung, D., and Körber, R. (2017). An ultra-sensitive and wideband magnetometer based on a superconducting quantum interference device. Appl. Phys. Lett. *110*, 072603. https://doi.org/10.1063/1.4976823.
17. Savukov, I., Kim, Y.J., and Schultz, G. (2020). Detection of ultra-low field NMR signal with a commercial QuSpin single-beam atomic magnetometer. J. Magn. Reson. *317*, 106780. https://doi.org/10.1016/j.jmr.2020.106780.
18. Roberts, G., Holmes, N., Alexander, N., Boto, E., Leggett, J., Hill, R.M., Shah, V., Rea, M., Vaughan, R., Maguire, E.A., et al. (2019). Towards OPM-MEG in a virtual reality environment. Neuroimage *199*, 408–417. https://doi.org/10.1016/j.neuroimage.2019.06.010.
19. Kominis, I.K., Kornack, T.W., Allred, J.C., and Romalis, M.V. (2003). A subfemtotesla multichannel atomic magnetometer. Nature *422*, 596–599. https://doi.org/10.1038/nature01484.
20. Shah, V.K., and Wakai, R.T. (2013). A compact, high performance atomic magnetometer for biomedical applications. Phys. Med. Biol. *58*, 8153–8161. https://doi.org/10.1088/0031-9155/58/22/8153.
21. Wyllie, R., Kauer, M., Smetana, G.S., Wakai, R.T., and Walker, T.G. (2012). Magnetocardiography with a modular spin-exchange relaxation-free atomic magnetometer array. Phys. Med. Biol. *57*, 2619–2632. https://doi.org/10.1088/0031-9155/57/9/2619.
22. Johnson, C., Schwindt, P.D.D., and Weisend, M. (2010). Magnetoencephalography with a two-color pump-probe, fiber-coupled atomic magnetometer. Appl. Phys. Lett. *97*, 243703. https://doi.org/10.1063/1.3522648.
23. Colombo, A.P., Carter, T.R., Borna, A., Jau, Y.Y., Johnson, C.N., Dagel, A.L., and Schwindt, P.D.D. (2016). Four-channel optically pumped atomic magnetometer for magnetoencephalography. Opt Express *24*, 15403–15416. https://doi.org/10.1364/OE.24.015403.
24. Wyllie, R., Kauer, M., Wakai, R.T., and Walker, T.G. (2012). Optical magnetometer array for fetal magnetocardiography. Opt. Lett. *37*, 2247–2249. https://doi.org/10.1364/OL.37.002247.
25. Boto, E., Holmes, N., Leggett, J., Roberts, G., Shah, V., Meyer, S.S., Muñoz, L.D., Mullinger, K.J., Tierney, T.M., Bestmann, S., et al. (2018). Moving magnetoencephalography towards real-world applications with a wearable system. Nature *555*, 657–661. https://doi.org/10.1038/nature26147.
26. Sulai, I.A., DeLand, Z.J., Bulatowicz, M.D., Wahl, C.P., Wakai, R.T., and Walker, T.G. (2019). Characterizing atomic magnetic gradiometers for fetal magnetocardiography. Rev. Sci. Instrum. *90*, 085003. https://doi.org/10.1063/1.5091007.
27. Guy, C.N., Cayless, A., and Walker, S. (1990). An analysis of gradiometer balancing procedures. Phys. Med. Biol. *35*, 741–753. https://doi.org/10.1088/0031-9155/35/6/004.
28. Tierney, T.M., Holmes, N., Mellor, S., López, J.D., Roberts, G., Hill, R.M., Boto, E., Leggett, J., Shah, V., Brookes, M.J., et al. (2019). Optically pumped magnetometers: From quantum origins to multi-channel magnetoencephalography. Neuroimage *199*, 598–608. https://doi.org/10.1016/j.neuroimage.2019.05.063.
29. Nardelli, N.V., Krzyzewski, S.P., and Knappe, S.A. (2019). Reducing crosstalk in optically-pumped magnetometer arrays. Phys. Med. Biol. *64*, 21NT03. https://doi.org/10.1088/1361-6560/ab4c06.
30. Holmes, N., Leggett, J., Boto, E., Roberts, G., Hill, R.M., Tierney, T.M., Shah, V., Barnes, G.R., Brookes, M.J., and Bowtell, R. (2018). A bi-planar coil system for nulling background magnetic fields in scalp mounted magnetoencephalography. Neuroimage *181*, 760–774. https://doi.org/10.1016/j.neuroimage.2018.07.028.
31. Grosz, A., Paperno, E., Amrusi, S., and Szpruch, T. (2010). Minimizing crosstalk in three-axial induction magnetometers. Rev. Sci. Instrum. *81*, 125106. https://doi.org/10.1063/1.3509392.
32. Lu, J., Wang, S., Lu, F., Lu, C., Zhang, X., and Ma, D. (2022). Hybrid optimal design of square highly uniform magnetic field coils. IEEE Trans. Ind. Electron. *70*, 4236–4244. https://doi.org/10.1109/TIE.2022.3179547.
33. Robinson, S.E., Andonegui, A.B., Holroyd, T., Hughes, K.J., Alem, O., Knappe, S., Maydew, T., Griesshammer, A., and Nugent, A. (2022). Cross-Axis Dynamic Field Compensation of Optically Pumped Magnetometer Arrays for MEG. Neuroimage *262*, 119559. https://doi.org/10.1016/j.neuroimage.2022.119559.
34. Jiang, M., Xu, W., Li, Q., Wu, Z., Suter, D., and Peng, X. (2020). Interference in atomic magnetometry. Adv. Quant. Technol. *3*, 2000078. https://doi.org/10.1002/qute.202000078.
35. Lin, S., Yuan, Z., Tang, J., Lu, J., Cao, Q., and Zhai, Y. (2023). Interaxial time-domain interference in single-beam SERF magnetometer. Measurement *215*, 112890. https://doi.org/10.1016/j.measurement.2023.112890.
36. Allred, J.C., Lyman, R.N., Kornack, T.W., and Romalis, M.V. (2002). High-sensitivity atomic magnetometer unaffected by spin-exchange relaxation. Phys. Rev. Lett. *89*, 130801. https://doi.org/10.1103/PhysRevLett.89.130801.
37. Dupont-Roc, J. (1970). Détermination par des méthodes optiques des trois composantes d'un champ magnétique très faible. Rev. Phys. Appl. *5*, 853–864. https://doi.org/10.1051/rphysap:0197000506085300.
38. Yuan, Z., Liu, Y., Xiang, M., Gao, Y., Suo, Y., Ye, M., and Zhai, Y. (2023). Compact multi-channel optically pumped magnetometer for bio-magnetic field imaging. Opt. Laser Technol. *164*, 109534. https://doi.org/10.1016/j.optlastec.2023.109534.
39. DeLand, Z.J. (2017). Advances in Fetal Magnetocardiography Using SERF Atomic Magnetometers (The University of Wisconsin-Madison).
40. Zhang, S., Zhang, K., Zhou, Y., Ye, M., and Lu, J. (2022). Triaxial precise magnetic field compensation of a zero-field optically pumped magnetometer based on a single-beam configuration. Opt Express *30*, 24579–24588. https://doi.org/10.1364/OE.464361.
41. Oostenveld, R., Fries, P., Maris, E., and Schoffelen, J.M. (2011). FieldTrip: open source software for advanced analysis of MEG, EEG, and invasive electrophysiological data. Comput. Intell. Neurosci. *2011*, 156869. https://doi.org/10.1155/2011/156869.
42. Hämäläinen, M., Hari, R., Ilmoniemi, R.J., Knuutila, J., and Lounasmaa, O.V. (1993). Magnetoencephalography-theory, instrumentation, and applications to noninvasive studies of the working human brain. Rev. Mod. Phys. *65*, 413–497. https://doi.org/10.1103/RevModPhys.65.413.
43. Gaho, A.A., Musavi, S.H.A., Jatoi, M.A., and Shafiq, M. (2018). EEG signals based brain source localization approaches. Int. J. Adv. Comput. Sci. App. *9*, 253–261. https://doi.org/10.14569/IJACSA.2018.090934.
44. Friston, K., Harrison, L., Daunizeau, J., Kiebel, S., Phillips, C., Trujillo-Barreto, N., Henson, R., Flandin, G., and Mattout, J. (2008). Multiple sparse priors for the M/EEG inverse problem. Neuroimage *39*, 1104–1120. https://doi.org/10.1016/j.neuroimage.2007.09.048.

STAR★METHODS

KEY RESOURCES TABLE

REAGENT or RESOURCE	SOURCE	IDENTIFIER
Software and algorithms		
Fieldtrip v20221210	Oostenveld et al. (2011)[41]	https://www.fieldtriptoolbox.org/download/
MATLAB vR2019b	MathWorks	https://ww2.mathworks.cn/products/matlab.html
Simulation algorithm	This paper	https://zenodo.org/doi/10.5281/zenodo.10584694

RESOURCE AVAILABILITY

Lead contact

Further information and requests for resources and reagents should be directed to and will be fulfilled by the lead contact, Ying Liu (liu_ying@buaa.edu.cn).

Materials availability

This study did not generate new unique reagents.

Data and code availability

- All data reported in this article will be shared by the lead contact on request.
- All original code has been deposited at Zenodo and is publicly available as of the date of publication. DOIs are listed in the key resources table.
- Any additional information required to reanalyze the data reported in this article is available from the lead contact upon request.

EXPERIMENTAL MODEL AND STUDY PARTICIPANT DETAILS

This study does not use experimental models typical in the life sciences.

METHOD DETAILS

Steady-state response of the dual-beam and single-beam modulated atomic magnetometer

The magnetometers' coordinates are shown in Figure S5. Whether it is dual-beam configuration or single-beam configuration the circularly polarized pump beam is defined on the *z*-axis. For dual-beam OPM, the external magnetic field to be sensed is defined on the *y*-axis and the linearly polarized probe beam is along the *x*-axis. For single-beam OPM, the sensitive axis is *x*-axis.

When the spin-exchange rate is much faster than the spin precession, the evolution of alkali-metal atomic ground state electron spin polarization $\mathbf{P}$ can be described by a Bloch equation as follows:[36]

$$\frac{d\mathbf{P}}{dt} = \frac{1}{q}\left[\Omega(t) \times \mathbf{P} + R_{op}(\hat{\mathbf{z}} - \mathbf{P}) - \Gamma\mathbf{P}\right], \quad \text{(Equation 5)}$$

where $\Omega(t) = \gamma\mathbf{B}(t)$, γ is the gyromagnetic ratio of the orbital electron, $\mathbf{B}(t) = [B_x(t), B_y(t), B_z(t)]$ is the external magnetic field, q is the slowing-down factor, R_{op} is the pumping rate, $\hat{\mathbf{z}}$ is the unit vector along the *z*-axis, Γ is the total relaxation rate except R_{op}. When the field to be measured is a static field, the electron spin polarization of the atomic ensemble in the vapor cell quickly reaches the steady state. Solving Equation 5 for $\frac{d\mathbf{P}}{dt} = 0$, we obtain

$$P_x = \frac{R_{op}}{\Gamma'\left(\Gamma'^2+\Omega_x{}^2+\Omega_y{}^2+\Omega_z{}^2\right)}\left(\Gamma'\Omega_y + \Omega_x\Omega_z\right), \quad \text{(Equation 6)}$$

$$P_y = \frac{R_{op}}{\Gamma'\left(\Gamma'^2+\Omega_x{}^2+\Omega_y{}^2+\Omega_z{}^2\right)}\left(-\Gamma'\Omega_x + \Omega_y\Omega_z\right), \quad \text{(Equation 7)}$$

$$P_z = \frac{R_{op}}{\Gamma'\left(\Gamma'^2+\Omega_x{}^2+\Omega_y{}^2+\Omega_z{}^2\right)}\left(\Gamma'^2 + \Omega_z{}^2\right), \quad \text{(Equation 8)}$$

where $\Gamma' = \Gamma + R_{op}$. For a dual-beam magnetometer, P_x (P_y) is only sensitive to B_y (B_x) when $B_z = 0$, but the z-component of the spin polarization P_z is non-sensitive to the external field. However, after applying a high-frequency modulation field $B_m \cos(\omega_m t)$ ($B_m \sim 150$ nT, $|\Omega| \ll \omega_m$) on the sensitive axis (x-axis), the first order harmonic response of P_z becomes as follows:[37]

$$P_z = 2\frac{R_{op}}{\Gamma'^2}J_0(u)J_1(u)\left[\frac{\Gamma'\Omega_x}{\Gamma'^2+\overline{\Omega}_0{}^2} + J_0(u)^2\frac{\overline{\Omega}_y\overline{\Omega}_z}{\Gamma'^2+\overline{\Omega}_0{}^2}\right], \quad \text{(Equation 9)}$$

where J_n is the nth order Bessel functions of the first kind; $\overline{\Omega}_0{}^2 = \gamma^2(B_x{}^2 + J_0(u)^2B_y{}^2 + J_0(u)^2B_z{}^2)$, $u = \gamma B_m/(q\omega_m)$. At this time P_z becomes sensitive to B_x in the near zero field environment. This is the operational principle of a single-beam modulated magnetometer.

We make two important observations comparing Equations 7 and 9: (1) the atomic magnetometer is simultaneously sensitive to the magnetic fields along the x and y axes when existing residual magnetic field on the pumping axis (B_z); (2) the response formulas of the spin polarization components of the probe axes of the single-beam and dual-beam magnetometers have the similar form. The first difference is that the demodulation of the first harmonic introduces attenuation of the amplitude. Another difference is that the presence of the modulation field modifies the precession frequency of the atom in weak fields. The modification depends on the relative orientation of the static field and the radio-frequency field. If these two fields are parallel, the Larmor frequency is unchanged; if, on the contrary, they are perpendicular, the Larmor frequency is multiplied by $J_0(u)$.[37]

Dynamic response of the dual-beam atomic magnetometer

We consider the operation of the OPM in a bias magnetic field along the pumping axis (B_z) and a small transverse oscillating magnetic field in x-y plane. We consider a general case of $\Omega(t) = [\Omega_x \cos(\omega_s t), \Omega_y \cos(\omega_s t), \Omega_z]$. Rewrite Equation 5 as a system of partial first-order, linear differential equations:[34]

$$\frac{dP_x}{dt} = \frac{1}{q}\left[\Omega_y(t)P_z - \Omega_z P_y - \Gamma' P_y\right], \quad \text{(Equation 10)}$$

$$\frac{dP_y}{dt} = \frac{1}{q}\left[\Omega_z P_x - \Omega_x(t)P_z - \Gamma' P_y\right], \quad \text{(Equation 11)}$$

$$\frac{dP_z}{dt} = \frac{1}{q}\left[\Omega_x(t)P_y - \Omega_y(t)P_x - \Gamma' P_z + R_{op}\right]. \quad \text{(Equation 12)}$$

From Equation 8 we know that in the weak magnetic field environment, the steady-state of P_z can be regarded as a constant $P_{z0} \approx R_{op}/\Gamma'$. Since the small transverse oscillating magnetic field will not deviate P_z much from P_{z0}, P_z can be replaced by P_{z0} in Equations 10 and 11. Combing the first two equations using Equation 10 $\pm$ i * Equation 11, one can derive

$$\frac{dP_\pm}{dt} = \frac{1}{q}\left[\pm i\Omega_z P_\pm - \Gamma' P_\pm \mp i\Omega_\pm(t)P_{z0}\right], \quad \text{(Equation 13)}$$

where $P_\pm = P_x \pm iP_y$, $\Omega_\pm(t) = \Omega_x(t) \pm i\Omega_y(t)$. The general solution to the above equation is

$$P_+(t) = e^{-\int\frac{\Gamma'-i\Omega_z}{q}dt}\left[C_1 + \int\frac{-iP_{z0}\Omega_+(t)}{q}e^{\int\frac{\Gamma'-i\Omega_z}{q}dt}dt\right]. \quad \text{(Equation 14)}$$

Since the term proportional to C_1 decays exponentially to zero very fast, Equation 14 becomes

$$P_+(t) = -i\frac{R_{op}}{\Gamma'}\frac{\Omega_{1+}\left[\omega_s q\sin(\omega_s t) + (\Gamma' - i\Omega_z)\cos(\omega_s t)\right]}{(\Gamma' - i\Omega_z)^2 + \omega_s{}^2q^2}, \quad \text{(Equation 15)}$$

where $\Omega_{1+} = \Omega_x + i\Omega_y$. The real part of Equation 15 represents $P_x(t)$ as follows

$$P_x(t) = \frac{R_{op}}{\Gamma'}\left[\Omega_y\frac{\sqrt{\Gamma'^2+\omega^2q^2}\cos(\omega_s t+\Phi_y)}{\sqrt{\left(\Gamma'^2 - \Omega_z{}^2+\omega_s{}^2q^2\right)^2+4\Gamma'^2\Omega_z{}^2}} + \Omega_x\frac{\Omega_z\cos(\omega_s t+\Phi_x)}{\sqrt{\left(\Gamma'^2 - \Omega_z{}^2+\omega_s{}^2q^2\right)^2+4\Gamma'^2\Omega_z{}^2}}\right], \quad \text{(Equation 16)}$$

where $\Phi_y = \arctan\left(\frac{-\omega_s q(\Gamma'^2+\omega_s{}^2q^2-\Omega_z{}^2)}{\Gamma'(\Gamma'^2+\omega_s{}^2q^2+\Omega_z{}^2)}\right)$, $\Phi_x = \arctan\left(\frac{-2\omega_s q\Gamma'}{\Gamma'^2-\omega_s{}^2q^2+\Omega_z{}^2}\right)$.

Dynamic response of the single-beam modulated atomic magnetometer

We now calculate the dynamic response of the single-beam modulated atomic magnetometer. We consider the case at first where the magnetic field along y- and z-axes are approximately zero, leading to a zero steady state of P_x. Combining Equations 11 and 12, one can derive:

$$\frac{dP_{\pm}}{dt} = \frac{1}{q}\left[-i\Omega_x(t)P_{\pm} - \Gamma' P_{\pm} + R_{op}\right], \quad \text{(Equation 17)}$$

where $P_{\pm} = P_z \pm iP_y$. Applying a modulation field with an amplitude of B_m at an angular frequency ω_m and assuming the amplitude of the field to be measured along the x-axis is B_x at an angular frequency ω_x ($\Omega_x \ll \Omega_m$). The general solution to Equation 17 can be expressed as:

$$P_+(t) = e^{-\int \frac{i(\Omega_x \cos(\omega_x t)+\Omega_m \cos(\omega_m t))+\Gamma'}{q}dt}\left[C_1 + \int \frac{R_{op}}{q} e^{\int \frac{i(\Omega_x \cos(\omega_x t)+\Omega_m \cos(\omega_m t))+\Gamma'}{q}dt}dt\right]. \quad \text{(Equation 18)}$$

Similarly, we ignore terms related to C_1. Using Bessel expansion $e^{iu\sin(\omega t)} = \sum_{k=-\infty}^{\infty} J_k(u)e^{ik\omega t}$, Equation 18 becomes as follows

$$\begin{aligned} P_+(t) = {} & \frac{R_{op}}{im'\omega_m q + in'\omega_x q + \Gamma'} e^{i(m'-m)\omega_m t + i(n'-n)\omega_x t} \\ & \times \sum_{m=-\infty}^{\infty}\sum_{m'=-\infty}^{\infty}\sum_{n=-\infty}^{\infty}\sum_{n'=-\infty}^{\infty} J_m(u_1)J_{m'}(u_1)J_n(u_2)J_{n'}(u_2), \end{aligned} \quad \text{(Equation 19)}$$

where $u_1 = \gamma B_m/(q\omega_m)$, $u_2 = \gamma B_x/(q\omega_x)$, $n' - n = \pm 1$. Since the higher-order resonance terms tend to zero, we only consider the dominant zero-order resonance term ($m' = 0$). Demodulating the response of the atomic magnetometer at the modulation frequency ($m = 1$), Equation 19 reduces to

$$\begin{aligned} P_+(t) &= 2R_{op}J_0(u_1)J_1(u_1)\sum_{n=-\infty}^{\infty}\sum_{n'=-\infty}^{\infty} J_n(u_2)J_{n'}(u_2)\frac{1}{in'\omega_x q + \Gamma'}e^{i(n'-n)\omega_x t} \\ &= 2R_{op}J_0(u_1)J_1(u_1)\sum_{n=-\infty}^{\infty}\sum_{n'=-\infty}^{\infty} J_n(u_2)J_{n'}(u_2)\frac{(\Gamma' - in'\omega_x q)\{\cos[\omega_x t(n'-n)] + i\sin[\omega_x t(n'-n)]\}}{\Gamma'^2 + (n'\omega_x q)^2}. \end{aligned} \quad \text{(Equation 20)}$$

Its real part is

$$\begin{aligned} P_z(t) &= 2R_{op}J_0(u_1)J_1(u_1)\sum_{n=-\infty}^{\infty}\sum_{n'=-\infty}^{\infty} J_n(u_2)J_{n'}(u_2)\frac{\Gamma'\cos[\omega_x t(n'-n)] + n'\omega_x q\sin[\omega_x t(n'-n)]}{\Gamma'^2 + (n'\omega_x q)^2} \\ &= 2R_{op}J_0(u_1)J_1(u_1)\sum_{n=-\infty}^{\infty}\sum_{n'=-\infty}^{\infty} J_n(u_2)J_{n'}(u_2)\frac{1}{\sqrt{\Gamma'^2 + (n'\omega_x q)^2}}\cos(\omega_x t(n'-n) + \theta_x), \end{aligned} \quad \text{(Equation 21)}$$

where $\theta_x = \arctan\left(-\frac{n'\omega_x q}{\Gamma'}\right)$.

The above equations give the analytical solution of the frequency response of the single-beam modulated atomic magnetometer to the sinusoidal oscillating field along the sensitive x-axis when $B_y = B_z = 0$. This formula is too complicated to calculate the specific response phase and amplitude. Combining the amplitude-frequency response and the phase-frequency response of the first-order low-pass filter and the numerical solution of the dual-beam magnetometer, we deduce that Equation 21 can be simplified as:

$$P_z(t) = 2J_0J_1R_{op}\frac{\Omega_x}{\Gamma'\sqrt{\Gamma'^2 + \omega_s^2 q^2}}\sin\left(\omega_x t + \arctan\left(-\frac{\omega_x q}{\Gamma'}\right)\right) = A_x\sin(\omega_x + \varphi_x), \quad \text{(Equation 22)}$$

where A_x represents the response amplitude and φ_x represents the response phase. To verify the accuracy of Equation 22, we use MATLAB to numerically simulate the amplitude-frequency response and phase-frequency response of the magnetometer represented by Equation 21 to different frequency signals, and compare the simulation results with the ones calculated by Equation 22, as shown in Figure S6.

Figure S6 proves the accuracy of our deduction. Thus, we further make an analogy and extend Equation 22 to a general situation according to the analysis in dynamic response of dual-beam atomic magnetometer. When existing static remanence in the pumping axis and the magnetic field to be measured has components on both the sensitive and non-sensitive axes, the frequency response of the single-beam modulated magnetometer can be inferred as

$$P_z(t) = 2J_0J_1\frac{R_{op}}{\Gamma'}\left[\Omega_x\frac{\sqrt{\Gamma'^2 + \omega_s^2 q^2}\cos(\omega_s t + \varphi_x)}{\sqrt{\left(\Gamma'^2 - J_0^2\Omega_z{}^2 + \omega_s^2 q^2\right)^2 + 4\Gamma'^2 J_0^2\Omega_z{}^2}} + \Omega_y\frac{J_0^2\Omega_z\cos(\omega_s t + \varphi_y)}{\sqrt{\left(\Gamma'^2 - J_0^2\Omega_z{}^2 + \omega_s^2 q^2\right)^2 + 4\Gamma'^2 J_0^2\Omega_z{}^2}}\right], \quad \text{(Equation 23)}$$

where $\varphi_x = \arctan\left(\frac{-\omega_s q(\Gamma'^2 + \omega_s^2 q^2 - J_0^2\Omega_z{}^2)}{\Gamma'(\Gamma'^2 + \omega_s^2 q^2 + J_0^2\Omega_z{}^2)}\right)$, $\varphi_y = \arctan\left(\frac{-2\omega_s q\Gamma'}{\Gamma'^2 - \omega_s^2 q^2 + J_0^2\Omega_z{}^2}\right)$.

When $B_y = B_z = 0$, Equation 23 is equal to Equation 22. To fully verify the accuracy of Equation 23, we use MATLAB to numerically solve the Bloch equation represented by Equations 6, 7, and 8. The simulation results are compared with the response signal calculated by Equation 23. The detailed comparisons of the amplitude and phase responses at different B_z, R_{op}, and Γ are shown in Figures S7–S11. The dots represent the numerical solutions of the Bloch equation and the lines represent the calculation results based on

our closed-form solution. The simulation results prove that Equation 23 is acceptable to be applied in the calculation and analysis of the dynamic response of the single-beam modulated OPM. The minor differences between numerical simulations and Equation 23 may be induced by the neglect of higher-order terms in the calculation process.

Sensor structure

The sensor depicted in Figure 1A consists of four magnetometers, each with a sensitivity of approximately 25 fT/ $Hz^{1/2}$ and a bandwidth of about 250 Hz. A single fiber is utilized to transmit pumping light for all four channels. The pumping beam, generated by a distributed Bragg reflector laser, was delivered to the sensor through a polarization-maintaining fiber. The spot diameter of the laser beam was expanded to 2.7 mm using a fiber collimator. Three identical combination prisms split the light emitted from the fiber into four beams of circularly polarized light directed into four ^{87}Rb vapor cells (each measuring 4× 4 × 4 mm^3 with a wall thickness of 0.5 mm). The incident light power for each channel was below 1 mW, and the light frequency was close to the resonance transition center of the ^{87}Rb D1 line. A three-axis rectangular Helmholtz coil set encircled each channel to produce a modulating magnetic field with an amplitude of approximately 150 nT at a frequency of 1 kHz, along with multi-axis static compensation fields.

Experimental apparatus

The sensor was located at the center of a five-layer magnetic shield (four μ-metal layers and one outermost aluminum layer) with a shielding factor of over 10^5. The experimental apparatus depicted in Figure 1B was employed to provide magnetic signals and record the response of the OPM. To measure the rotation of the sensitive axis in the presence of a static magnetic field along the pumping axis, a triaxial coil set embedded in the magnetic shield was driven by a commercial digital-to-analog converter (National Instruments, PXIe-4463) to generate a rotating magnetic field with an effective value of 100 pT at an angle θ with respect to the x-axis in the x-y plane across a frequency range of 10-200 Hz. Another set of shield coils was used to generate B_z. The photodiode currents of the OPM were fed to a transimpedance-amplifier (Thorlabs) and then filtered using a low-pass filter (Stanford Research Systems). A lock-in amplifier (Zurich Instruments) demodulated the filtered signal at ω_m and the signal was acquired by a commercial data-acquisition system (National Instruments, PXIe-4464). The commercial instruments used in the experiment can only test the performance of one OPM. Therefore, a four-channel electronic control system developed by the authors was also employed, which enabled two OPMs to operate simultaneously. The control system integrated the functions of temperature control, magnetic field compensation, modulation, and demodulation. Moreover, the residual magnetic field in the propagation axis of the laser of each OPM was adjusted using the host computer of the control system.[38] As the response signals of each OPM are processed by a signal processing system with identical models and configurations, the phase delay introduced by the signal processing system remains the same for each OPM. The impact of the signal processing system on the results of gradient difference can be ignored.

QUANTIFICATION AND STATISTICAL ANALYSIS

The random static magnetic fields with Gaussian distribution along the laser propagation axis are generated by MATLAB, and the gradient error mean values are calculated by Microsoft Excel.